

Low-Crystalline Bimetallic Metal–Organic Framework Electrocatalysts with Rich Active Sites for Oxygen Evolution

Jiantao Li,^{†,#} Wenzhong Huang,^{†,#} Manman Wang,[†] Shibo Xi,[‡] Jiashen Meng,[†] Kangning Zhao,^{†,§} Jun Jin,[§] Wangwang Xu,^{||} Zhaoyang Wang,[†] Xiong Liu,[†] Qiang Chen,[†] Linhan Xu,[⊥] Xiaobin Liao,[†] Yalong Jiang,[†] Kwadwo Asare Owusu,[†] Benli Jiang,[†] Chuanxi Chen,[†] Danian Fan,[†] Liang Zhou,^{*,†,§} and Liqiang Mai^{*,†,§}

[†]State Key Laboratory of Advanced Technology for Materials Synthesis and Processing, International School of Materials Science and Engineering, Wuhan University of Technology, Wuhan 430070, Hubei, China

[‡]Institute of Chemical and Engineering Sciences, A*STAR, 1 Pesek Road, Jurong Island 627833, Singapore

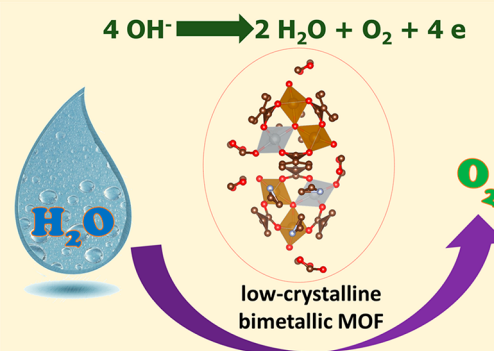
[§]School of Chemical and Biomedical Engineering, Nanyang Technological University, 50 Nanyang Avenue, Singapore 639798, Singapore

^{||}Department of Mechanical & Industrial Engineering, Louisiana State University, Baton Rouge, Louisiana 70803, United States

[⊥]Department of Physics and Collaborative Innovation Center for Optoelectronic Semiconductors and Efficient Devices, Xiamen University, Xiamen 361005, Fujian, China

Supporting Information

ABSTRACT: Developing efficient, stable, and low-cost catalysts for oxygen evolution reaction (OER) is highly desired in water splitting and metal–air batteries. Transition metal–organic frameworks (MOFs) have emerged as promising catalysts and have been intensively investigated especially due to their tunable crystalline structure. Unlike traditional strategies of tuning the morphology of well-crystalline MOFs, low-crystalline bimetallic MOFs are constructed via inducing exotic metal ions, and the formation process is revealed by experimental and theoretical methods. The low-crystalline bimetallic MOFs exhibit rich active sites due to local crystallinity and long-range disorder and deliver a small overpotential of 260 mV at 10 mA cm⁻², a low Tafel slope of 35 mV dec⁻¹, and a high Faradaic efficiency of 99.5% as oxygen evolution electrocatalysts. The work opens up a new avenue for the development of highly efficient earth-abundant catalysts in frontier potential applications.



The growing energy demand and fast depletion of fossil fuels are greatly stimulating the development of clean energy conversion and storage technologies.¹ Water splitting is regarded as a promising option to solve the energy crisis but limited by the bottleneck of oxygen evolution reaction (OER), involving multistep proton-coupled electron transfer and relatively sluggish kinetics.^{2,3} To date, precious IrO₂ and RuO₂ nanomaterials are considered as the most efficient OER electrocatalysts because of their intrinsic high activity.⁴ However, the limited resource and high cost greatly restrict their large-scale practical applications. During the past two decades, extensive efforts have been paid to the development of efficient earth-abundant and low-cost alternatives. Especially, first-row transition metal-based OER catalysts, including metal oxides, (oxy)hydroxides, carbides,

phosphides, sulfides, and nitrides, have been widely studied.^{5–11} Some efficient strategies including morphology modulation, surface modification, nanoscale composition with conductive materials, and construction of bi/multimetallic components have been carried out to improve the electrocatalytic performances. For example, Zhang et al.¹² reported NiFe layered double hydroxide deposited on Co,N-co-doped carbon nanoframes with rapid mass transport and superior electron transfer, displaying a small overpotential of 312 mV at 10 mA cm⁻² in alkaline conditions, which surpasses most of traditional transition metal-based catalysts. By constructing

Received: December 1, 2018

Accepted: December 18, 2018

Published: December 18, 2018

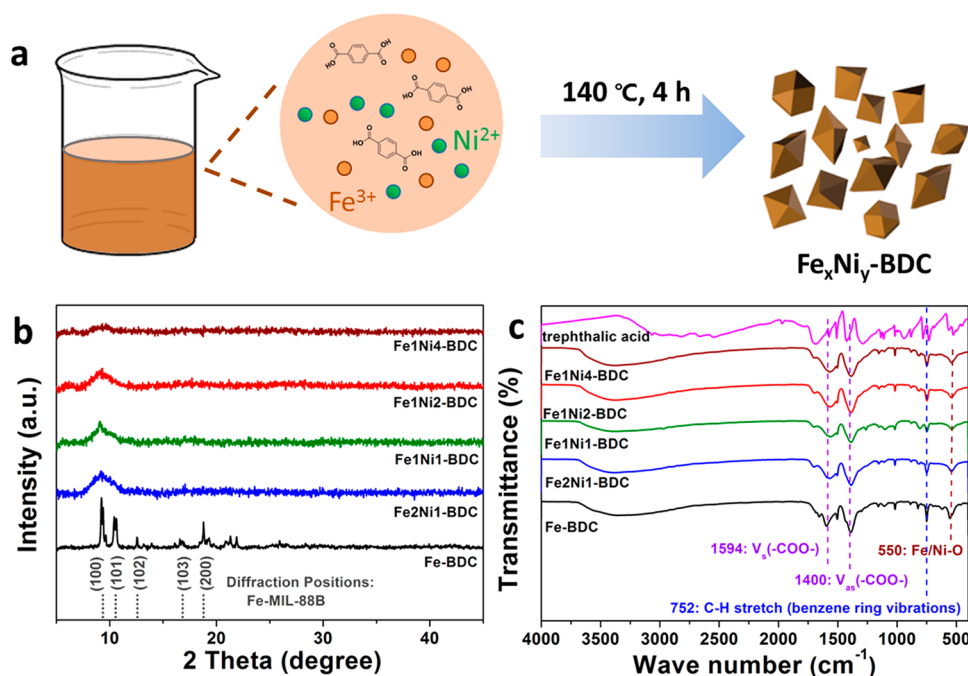


Figure 1. (a) Scheme for the synthesis of $\text{Fe}_x\text{Ni}_y\text{-BDC}$, (b) XRD patterns of Fe-BDC, Fe₂Ni₁-BDC, Fe₁Ni₁-BDC, Fe₁Ni₂-BDC, and Fe₁Ni₄-BDC (diffraction positions of Fe-MIL-88B are shown in the bottom), and (c) their corresponding FT-IR spectra compared with the spectrum of H₂BDC.

from interconnected ultrathin Ni–Fe layered double hydroxide (LDH) nanosheets, Lou et al.¹³ put forward a self-templated strategy to prepare Ni–Fe LDH hollow nanoprisms with excellent performance (an overpotential of 280 mV at 10 mA cm⁻²), which is attributed to the open porous structure and synergistic effects between Ni and Fe. As known, the electrocatalytic process of OER happens on the surface of catalysts; however, regardless of the wide study and significant progress of OER catalysts, the intrinsic activity and number of active sites are still limited. Therefore, rational design of new efficient OER catalysts with rich active sites on the whole structure rather than on a shallow surface remains a great challenge.

Metal–organic frameworks (MOFs), a new class of crystalline materials, are formed by coordination reactions between metal clusters/ions and organic ligands.¹⁴ MOFs have emerged as promising catalysts for broader applications especially due to their tunable crystalline structure.^{15–18} However, the good crystallinity of MOFs is a double-edged sword because the active sites are finely confined in the crystalline frameworks, which is not good for the OER process occurring on the surface. Recently, to solve the above-mentioned issues, an efficient nanoscale and morphology modulation method was utilized to design and construct unique MOF nanostructures. For instance, with judicious considerations of the host/guest geometries and modular synthetic strategies, Zhang et al.¹⁹ have immobilized and stabilized the labile dicobalt clusters in a MOF as coordinative guests and further obtained Fe₃-Co₂@GC electrodes with a 283 mV overpotential at 10 mA cm⁻² in water at pH = 13. Zhao et al.²⁰ developed a facile chemical bath deposition strategy to construct an ultrathin MOF nanosheet array on various substrates with superior OER properties, which were attributed to the highly exposed active molecular metal sites, improved electrical conductivity, and hierarchical porosity.

Looking beyond the great improvement of electrocatalytic OER performance based on nanoscale MOFs, the easy aggregation, relatively low yield, and low mass loading limit their practical applications. In this regard, developing efficient strategies to endow the bulk MOF structures at a high yield with full active sites and fast mass transport are highly desired.

Herein, we report a facile strategy to fabricate low-crystalline bimetallic (Fe/Ni) MOF nanoparticles by controlling the coordination reaction between Fe/Ni ions and terephthalic acid (H₂BDC) during the solvothermal process (the final products are denoted as $\text{Fe}_x\text{Ni}_y\text{-BDC}$). The coordination mechanism is clearly revealed through experimental analysis and density functional theory (DFT) calculations. It is found that the introduction of Ni ions would result in mismatched coordination with organic ligands, thus resulting in the loss of long-range order structure. The resulting architecture possesses rich defects with local crystallinity, which greatly improves mass transport and increases efficient active sites. When employed as an OER catalyst, the $\text{Fe}_x\text{Ni}_y\text{-BDC}$ nanoparticles could afford a low overpotential of 260 mV (at a current density of 10 mA cm⁻²) and a high turnover frequency of 0.36 s⁻¹ at 330 mV in alkaline solution, which outperforms most traditional crystalline inorganic materials. We believe that the development of this kind of original effective and durable low-crystalline catalysts could really help solve the bottleneck problem of water oxidation.

The formation process of low-crystalline $\text{Fe}_x\text{Ni}_y\text{-BDC}$ nanopolyhedrons is illustrated in Figure 1a. The feeding ratio of Fe/Ni is kept at 1/0, 2/1, 1/1, 1/2, 1/4, and 0/1. During the solvothermal process, the metal ions coordinate with the terephthalic acid ions through a coprecipitation process, and then $\text{Fe}_x\text{Ni}_y\text{-BDC}$ MOFs nanopolyhedrons are formed.

X-ray diffraction (XRD) was carried out to detect the structure evolution of $\text{Fe}_x\text{Ni}_y\text{-BDC}$ samples along with variation of the Fe/Ni ratio (Figure 1b). Significantly, the

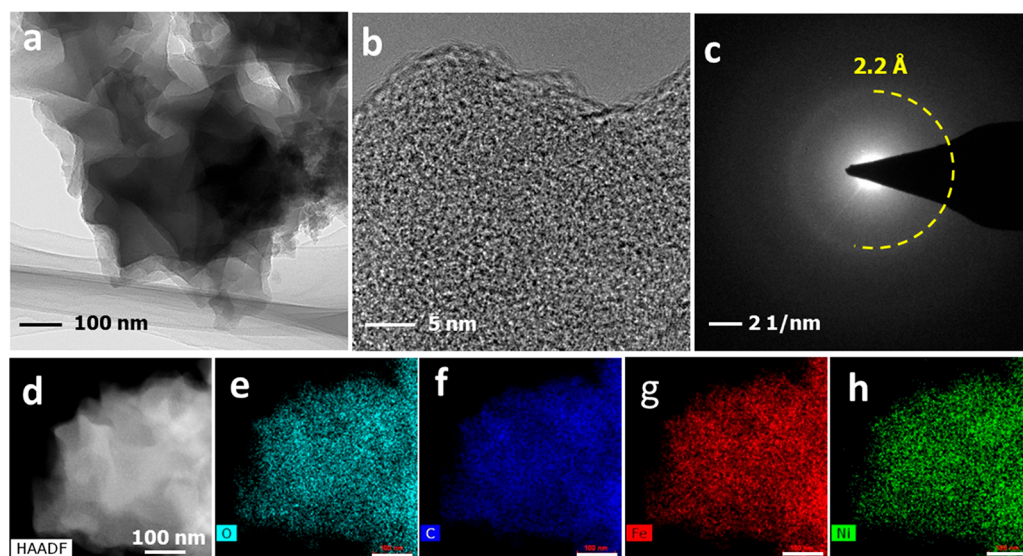


Figure 2. (a) TEM image, (b) HRTEM image, (c) SAED pattern, (d) HAADF-STEM image, and (e–h) corresponding EDX elemental maps of Fe1Ni2-BDC (scale bar dimensions in (e–h) are all 100 nm).

Fe-BDC shows high crystallinity with characteristic reflections of (100) at about 9.3° and (101) at about 10.5° , which are indexed to Fe-MIL-88B phase.^{21,22} However, a broad “hump” appears at around 10° and becomes smaller along with a decreasing Fe/Ni ratio. The poor XRD total diffraction peaks indicate that the Fe_xNi_y-BDC samples have low crystallinity. When the feeding molar ratio of Fe is smaller than 50%, the diffraction peak finally disappears. These phenomena could be ascribed to the introduction of Ni²⁺ ions, which would change the distribution of the local electrons and lead to the aperiodic arrangements of atoms.¹⁴

To detect the functional groups of Fe_xNi_y-BDC, Fourier transform infrared (FT-IR) spectroscopy was carried out in the range of 4000–400 cm⁻¹ (Figure 1c). The peak at 752 cm⁻¹ elucidates the vibration of C–H bonding inside of the benzene ring.²³ The peak at 550 cm⁻¹ is attributed to the bond between metal atoms (Fe and Ni) and the carboxylic (O–C=O) groups of BDC.²⁴ The presence of metal–oxygen bonds signifies that the coordination has been successfully built between the organic linkers and metal (Fe/Ni) ions. Furthermore, the peaks at around 1400 and 1594 cm⁻¹ correspond to the $\nu_{as}(-\text{COO}-)$ and $\nu_s(-\text{COO}-)$ of coordination bonds between the organic ligands and the metal centers.^{24,25} It can also be inferred that the existence of the hydrophilic carboxylate groups could enhance the availability of water (H₂O) to adsorb on the surface of Fe_xNi_y-BDC materials, which is beneficial to the OER process. Besides, the Raman spectra were also employed to characterize the pristine sample. In Figure S1, the pristine sample presents the benzene ring stretching mode that corresponds to C–H at 858, 810, and 628 cm⁻¹.^{24,26} Additionally, the peaks at around 1611 and 1434 cm⁻¹ are assigned to the stretching region of the in- and out-of-phase carboxylate group, respectively, and the peak at 1137 cm⁻¹ also associates with the vibration of terephthalic acid.²⁴ All of the above results clearly confirm the successful coordination between metal ions and terephthalic acid ions.

Additionally, the morphology of Fe1Ni2-BDC was identified with scanning electron microscopy (SEM) and transmission electron microscopy (TEM). The Fe1Ni2-BDC presents the

morphology resembling nanopolyhedrons (Figure 2a), and no obvious lattice fringes are observed (Figure 2b), suggesting the formation of low crystallinity. The selected area electron diffraction (SAED) pattern only shows ambiguous wings, suggesting the existence of local crystallinity (Figure 2c), which is consistent with the property of long-range disorder but short-range order. In addition, the high-angle annular dark field scanning transmission electron microscopy (HAADF-STEM, Figure 2d) and energy dispersive X-ray (EDX) test (Figure 2e–h) display a uniform distribution of O, C, Fe, and Ni elements. Meanwhile, inductively coupled plasma optical emission spectroscopy (ICP-OES) was employed to analyze the ratio change of Fe/Ni (Figure S2). It is observed that the elemental ratio of Fe/(Fe + Ni) measured from ICP is not the same as that of feeding ratio, while the ratio trends are consistent with each other: the value of Fe/(Fe + Ni) decreases with the addition of Ni. The phenomenon resulted from the fact that the Ni²⁺ ions are not that easy to coordinate with BDC ligands as Fe³⁺ ions, and some of the Ni²⁺ ions will not participate in the coordination process but are left in the solution and washed away finally. The SEM images of all Fe_xNi_y-BDC samples show that with the decrement of the Fe/Ni molar ratio, the average particle size decreases from the microscale (Fe-BDC) to nanoscale (Fe1Ni4-BDC) and the shapes gradually transform from an octahedron (Fe-BDC) to irregular shape (Fe_xNi_y-BDC) (Figure S3). However, when the molar ratio of Fe/Ni is 0/1, no product is obtained after the solvothermal process (Figure S4), suggesting that Ni²⁺ could not directly coordinate with BDC under the condition that we applied (solvothermal treatment under 140 °C for 4 h). The morphology change is mainly derived from the introduction of Ni²⁺ ions, which may affect the coordination between Fe³⁺ ions and BDC ligands, and result in the mismatch of metal–ligands, thus leading to long-range disorder and morphology change.

The XPS spectra of pristine Fe-BDC, Fe1Ni2-BDC, and Fe1Ni4-BDC are given in Figure S5. The XPS survey spectra of all samples (Figure S5a) proves the existence of Fe, Ni, C, and O elements. In addition, high-resolution XPS spectra of Ni 2p, Fe 2p, O 1s, and C 1s are shown in Figure S5b–e. The Ni

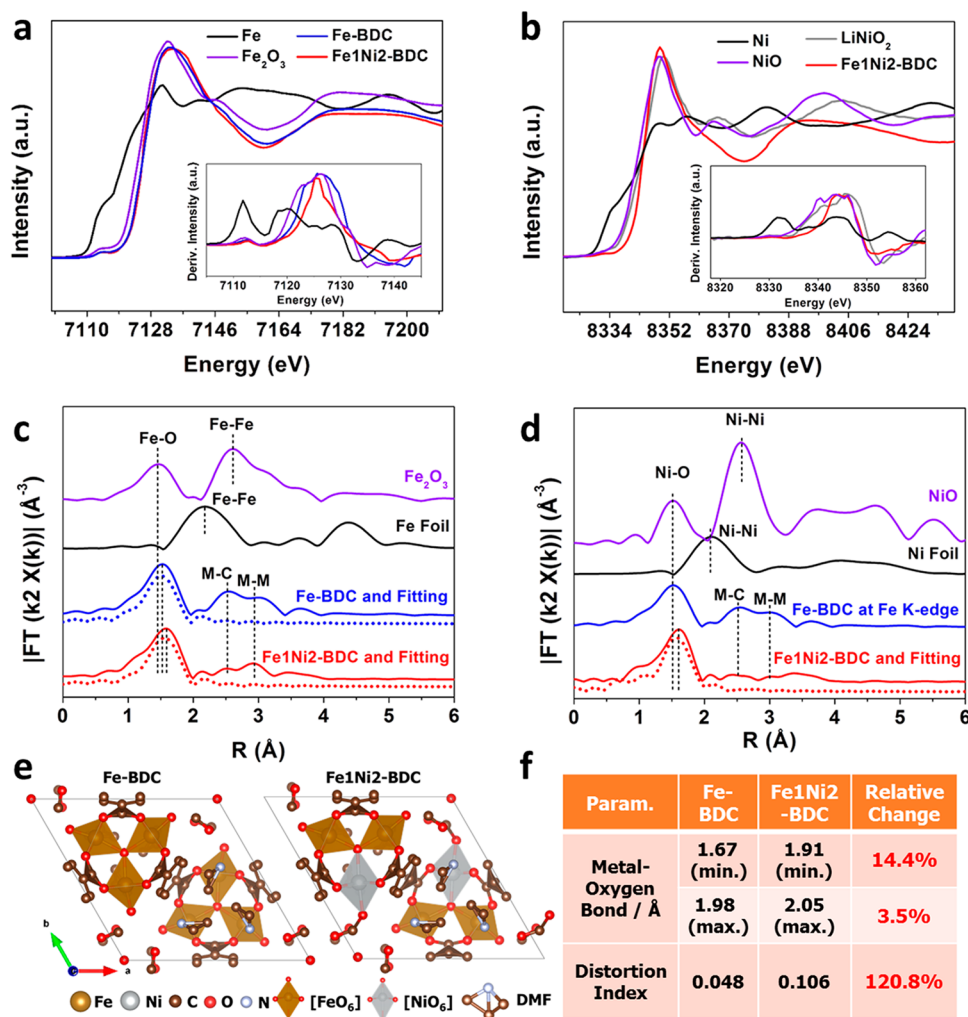


Figure 3. (a) Fe K-edge XANES and (c) Fourier-transformed EXAFS spectra of Fe-BDC, Fe1Ni2-BDC, and their references. (b) Ni K-edge XANES and (d) Fourier-transformed EXAFS spectra of Fe1Ni2-BDC and its references. Insets in (a) and (b) are the corresponding first derivative XANES data, and dashed lines in (c) and (d) are the corresponding fitting curves. (e) DFT calculations on the crystal structure of Fe-BDC (Fe-MIL-88B) and Fe1Ni2-BDC (using Ni²⁺ to partially replace Fe³⁺ in the octahedral structure). (f) Comparisons of crystal structure parameters between Fe-BDC and Fe1Ni2-BDC. It should be pointed out that the actual ratio of Fe/Ni measured by ICP is about 2.3; therefore, in the model of Fe1Ni2-BDC (named after the feeding ratio not the measured ratio), the ratio of Fe/Ni was kept as 2.0.

2p XPS spectra (Figure S5b) show the characteristic spin-orbit peaks of the Ni²⁺. The binding peak at around 856.1 eV (Ni 2p_{3/2}) is attributed to the existence of Ni–oxygen bonds,²⁷ and the peak at around 861.3 eV (Ni 2p_{3/2}) is the satellite of Ni 2p_{3/2}. For Fe XPS spectra (Figure S5c), the peak at around 711.9 eV (2p_{3/2}) is assigned to the Fe³⁺ oxidation state,¹⁶ and the peak at 717.3 eV (Fe 2p_{3/2}) belongs to the satellite. High-resolution C 1s XPS spectra (Figure S5d) are fitted by three surface components, namely, the BDC benzoic ring (284.7 eV), the C–O (285.8 eV), and the carboxylate (O–C=O) group of BDC (288.8 eV).^{24,25,28} In Figure S5e, the O 1s XPS spectra can be deconvoluted into three energy peaks at 532.7, 531.9, and 531.1 eV, which are ascribed to the absorbed water, the carboxylate groups of the BDC linkers, and Fe(Ni)–O bonds, respectively.²⁵ The XPS results above indicate that, though there is an increase of low crystallinity from Fe-BDC to Fe1Ni4-BDC, the chemical states and coordination environment of different elements are kept, suggesting that the same incorporation of metal ions and BDC ligands exists in all samples, which is consistent with the characteristic of local crystallinity.

To further verify the coordination structure and chemical state of Fe_xNi_y-BDC, X-ray absorption fine structure (XAFS) analysis was carried out. Figure 3a shows the X-ray absorption near-edge structure (XANES) spectra of Fe-BDC, Fe1Ni2-BDC, and their reference samples at Fe K-edge. It is observed that Fe-BDC and Fe1Ni2-BDC have the same response signal around the near-edge, revealing an identical chemical structure of Fe. From the first derivative XANES data (inset in Figure 3a), it can be seen that the E₀ values (the first inflection point on the absorption edge) at the Fe K-edge of Fe-BDC and Fe1Ni2-BDC are both at 7125.6 eV, almost equaling that of Fe₂O₃ (7126.0 eV, Fe³⁺) and much larger than that of Fe (7111.8 eV, Fe⁰), confirming the valence state of Fe³⁺. The Ni K-edge XANES spectra (Figure 3b) show that Ni in Fe1Ni2-BDC has a near-edge peak similar to that of NiO. As shown in the inset of Figure 3b, the E₀ value at the Ni K-edge of Fe1Ni2-BDC (8344.2 eV) is close to that of NiO (8343.8 eV, Ni²⁺), while it is larger than that of Ni foil (8331.5 eV, Ni⁰) and smaller than that of LiNiO₂ (8345.4 eV, Ni³⁺), thus indicating that the valence state of Ni in Fe1Ni2-BDC is approaching Ni²⁺.

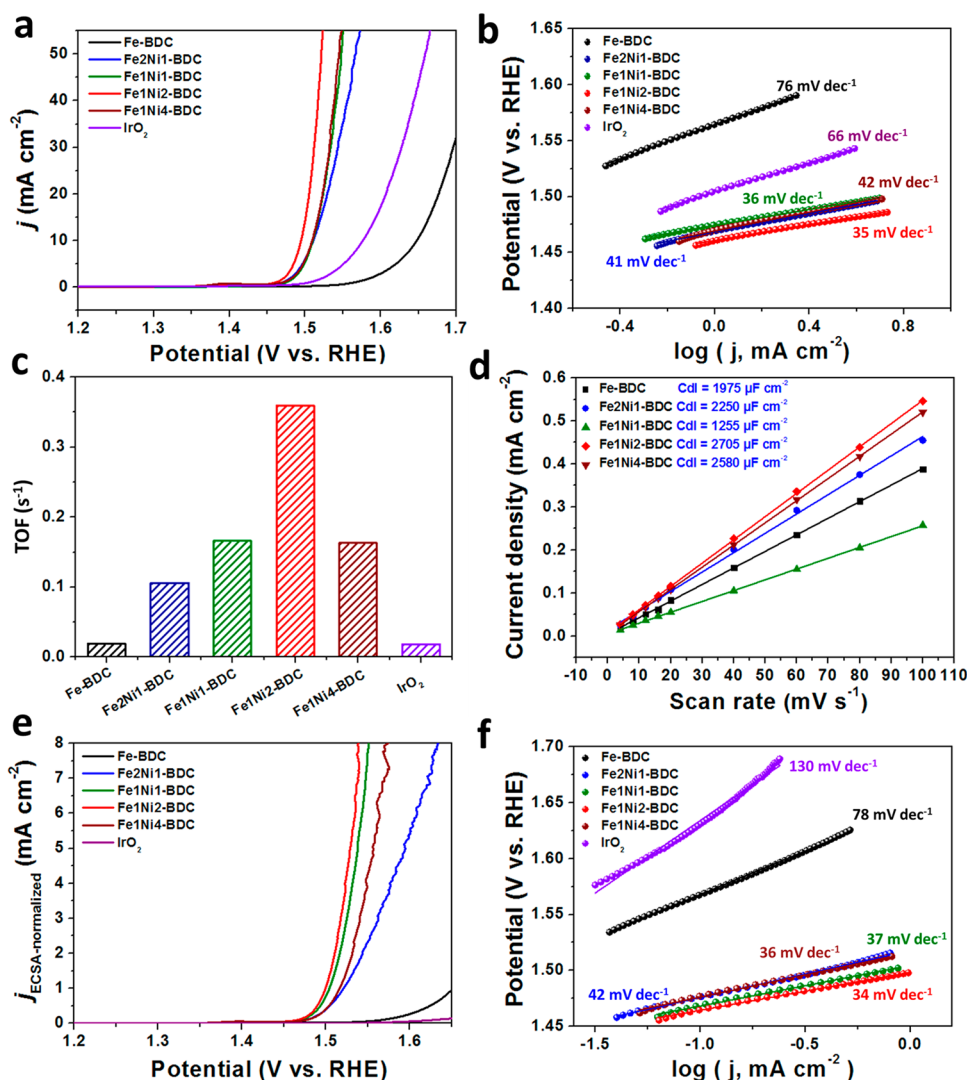


Figure 4. (a) LSV curves of Fe-BDC, Fe₂Ni₁-BDC, Fe₁Ni₁-BDC, Fe₁Ni₂-BDC, Fe₁Ni₄-BDC, and IrO₂ in 1 M KOH at a scan rate of 5 mV s⁻¹. (b) Tafel plots of different catalysts. (c) TOF values calculated at an overpotential of 330 mV. (d) CV current density versus scan rate for different catalysts; the linear slope is equivalent to the double-layer capacitance (C_{dl}). (e) LSV curves of Fe-BDC, Fe₂Ni₁-BDC, Fe₁Ni₁-BDC, Fe₁Ni₂-BDC, Fe₁Ni₄-BDC, and IrO₂ normalized by ECSA ($j_{ECSA-normalized}$) and (f) Tafel plots which also normalized by ECSA ($j_{ECSA-normalized}$) of different catalysts.

The Fourier-transformed extended X-ray absorption fine structure (EXAFS) spectra in the R space (Figure 3c,d) are presented without phase correction. As shown in Figure 3c, both the prominent peaks of Fe-BDC (1.52 Å) and Fe₁Ni₂-BDC (1.57 Å) are very close to that of Fe₂O₃ (1.47 Å), whose building blocks are [FeO₆] octahedra; thus, it can be preliminarily inferred that Fe in Fe-BDC and Fe₁Ni₂-BDC have an octahedral coordination configuration. Further, the EXAFS spectra for Fe-BDC and Fe₁Ni₂-BDC at the Fe/Ni K-edge were fitted based on the models of Fe-MIL-88B and Fe₁Ni₂-MIL-88B (Figure 3e). The coordination numbers of Fe–O and Ni–O are unified at 6 during the fitting process, and the fitting curves (dashed lines in Figure 3c,d) are consistent with corresponding experimental EXAFS profiles, suggesting the successful formation of [FeO₆] and [NiO₆] octahedral configurations in both Fe-BDC and Fe₁Ni₂-BDC (detailed fitting results are summarized in Table S2).

The metal–metal (M–M) peaks in both Fe and Ni K-edge EXAFS spectra of Fe-BDC and Fe₁Ni₂-BDC become much weaker compared with those of metal foils and metal oxides,

and the reason is that the size of BDC ligands is relatively large, which results in the long distance between metal atoms; thus, the effective scattering signal between metals will become weakened. Besides, the Ni–Ni peak intensity is much lower than that of the Fe–Fe peak, suggesting that the introduction of Ni²⁺ ions will also increase the disorder degree. The phenomenon above demonstrates that Fe³⁺ and Ni²⁺ ions are successfully coordinated with BDC ligands, and the introduction of Ni²⁺ ions will absolutely affect the original structure of Fe-BDC and may further lead to the formation of long-range disorder. Moreover, the Ni–O distance ($R = 1.62$ Å) is larger than that of Fe–O ($R = 1.52$ Å) in Fe₁Ni₂-BDC, and there is even a small increase in the Fe–O bond itself when introducing Ni²⁺ ions into the framework of Fe-BDC, which may be caused by the larger radius of the Ni²⁺ ion than that of the Fe³⁺ ion in the environment of octahedral coordination and the weaker electrostatic attraction to negatively charged ligands (the phenomenon above can be checked as summarized in a previous report²⁹); meanwhile, the elongation of the Fe–O bond itself may also be affected by coordination between Ni²⁺

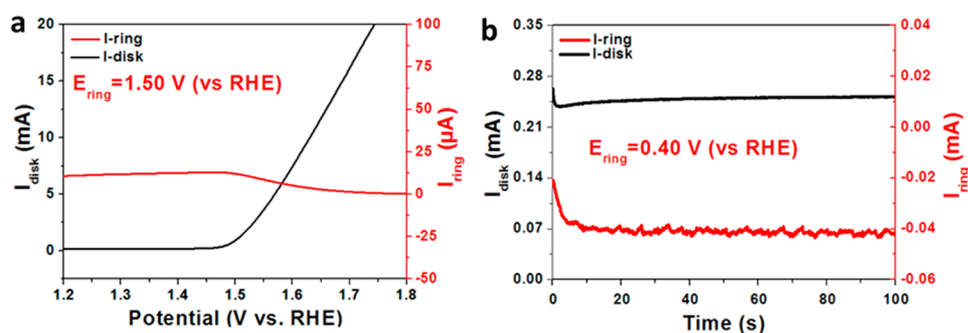


Figure 5. (a) Disk and ring current of Fe1Ni2-BDC tested on RRDE in a 1 M KOH solution with a ring potential of 1.50 V (1000 rpm; 5 mV s^{-1}). (b) Disk and ring current of Fe1Ni2-BDC tested on RRDE (1000 rpm) in a N_2 -saturated 1 M KOH solution with a ring potential of 0.40 V (1000 rpm).

ions and BDC ligands, which is likely to result in long-range disorder.

DFT calculations were performed to further investigate the effect on the introduction of Ni^{2+} on crystalline Fe-MIL-88B (Figure 3e,f). Fe-MIL-88B is constructed by terephthalic acid and $[\text{FeO}_6]$ octahedra, displaying a hexagonal three-dimensional structure and tunnels along the c axis. After one-third of $[\text{FeO}_6]$ octahedra were replaced by $[\text{NiO}_6]$ octahedra, the minimum metal–oxygen bonds change from 1.67 to 1.91 Å (maximum from 1.98 to 2.05 Å), the increase in the bond length after introducing Ni^{2+} ions is consistent with the results of EXAFS analysis, and the distortion index of the $[\text{MO}_6]$ octahedron also changes from 0.048 to 0.106. It can be inferred that the large relative changes of bond length (14.4%) and distortion index (120.8%) result in the loss of long-range order in Fe1Ni2-BDC. Therefore, the introduction of Ni^{2+} ions into Fe-MIL-88B plays an important role in the formation of the low-crystalline Fe x Ni y -BDC.

The electrocatalytic OER performance of the as-synthesized samples and commercial IrO_2 was measured in a 1 M KOH aqueous solution. Linear sweep voltammetry (LSV) curves were scanned at a rate of 5 mV s^{-1} (Figure 4a), and LSV curves showed that Fe1Ni2-BDC needs the lowest overpotential of 260 mV to derive a current density of 10 mA cm^{-2} , much smaller than those of Fe-BDC (419 mV), Fe2Ni1-BDC (280 mV), Fe1Ni1-BDC (281 mV), Fe1Ni4 (280 mV), and commercial IrO_2 (340 mV). OER kinetics was analyzed by Tafel plots. As shown in Figure 4b, the measured Tafel slopes are 76, 41, 36, 35, 42, and 66 mV dec^{-1} for Fe-BDC, Fe2Ni1-BDC, Fe1Ni1-BDC, Fe1Ni2-BDC, Fe1Ni4-BDC, and IrO_2 . It shows that Fe2Ni1-BDC possesses the lowest Tafel slope, corresponding to the fastest kinetics among all of the samples. The corresponding electrocatalytic parameters of Fe x Ni y -BDC are summarized in Table S3, and the performance obtained in Fe1Ni2-BDC also outperforms most of the remarkable OER catalysts reported to date, as shown in Table S4.

To investigate the average activity of a single active site, the turnover frequency (TOF) was calculated based on the active site number (see details in the Supporting Information and Figure S6). If we assume that all of the metal ions loaded on the electrode take part in the electrocatalytic process, then the highest TOF of 0.36 s^{-1} for Fe1Ni2-BDC can be achieved at an overpotential of 330 mV (Figure 4c). If the active site number is measured from cyclic voltammetry (CV) curves, Fe1Ni2-BDC still possess the highest TOF value (see the Supporting Information, Table S1), suggesting that a highly

active single site can be achieved by introducing a proper ratio of Ni^{2+} ions into Fe-BDC.

Electrochemically active areas (ECSAs) were evaluated from the double-layer capacitance (C_{dl}) by measuring CV in the non-Faradaic region (see details in the Supporting Information and Figure S7). Figure 4d shows that the C_{dl} value of Fe1Ni2-BDC is 2.70 mF cm^{-2} , much larger than those of Fe-BDC (1.98 mF cm^{-2}), Fe2Ni1-BDC (2.25 mF cm^{-2}), Fe1Ni1-BDC (1.26 mF cm^{-2}), and Fe1Ni4-BDC (2.58 mF cm^{-2}). It should be pointed out that the tested C_{dl} of IrO_2 (Figure S8) is very high (28.7 mF cm^{-2}), possibly due to the size effect of nanocrystals.³⁰ For the as-synthesized samples, Fe1Ni2-BDC with the highest C_{dl} value has the best performance, implying that the electrocatalytic OER activity is relevant to the larger ECSA, which can contribute to an effective electrode–electrolyte interface area and more exposed active sites.

Electrochemical impedance spectroscopy (EIS) was also acquired to further illustrate the fast reaction kinetics. The value of charge transfer resistance (R_{ct}) has a positive correlation with reaction kinetics as a smaller R_{ct} value can lead to faster charge transfer.³¹ As shown in Figure S9a, Fe1Ni2-BDC exhibits the smallest R_{ct} of about 2.29 ohm among all of the samples, which can ensure a much faster charge transfer on the interface between the electrode and electrolyte, thus resulting in enhanced electrocatalytic performance. The improved charge transfer capability can be mainly attributed to the low-crystalline or even amorphous structure, which can help to accelerate transport of charged species in the interface between the catalyst and electrolyte.^{32,33} The long-term durability of Fe1Ni2-BDC was also evaluated. As shown in Figure S9b, the chronopotentiometric curve measured at 10 mA cm^{-2} shows that almost no potential polarization can be observed after 10 h, suggesting the impressive electrocatalytic stability of Fe1Ni2-BDC.

What's more, to investigate the intrinsic activity of catalysts (i.e., to eliminate the contribution from ECSA), LSV curves and Tafel plots normalized by ECSA were also provided (Figure 4e,f). The value of ECSA is calculated by dividing C_{dl} using a standard specific capacitance value (see details in the Supporting Information). As reported by Xu et al.,³⁴ normalization of the current density by ECSA is more reliable to study the intrinsic activity. After ECSA normalization, Fe1Ni2-BDC still possesses the smallest overpotential (300 mV at 5 mA cm^{-2}) and the lowest Tafel slope (34 mV dec^{-1}). Results above reveal that Fe1Ni2-BDC possesses the best intrinsic performance, which is consistent with the single-site activity evaluated by the TOF.

The enhanced catalytic performance for Fe1Ni2-BDC is believed to be derived from the following factors. First, the introduction of Ni²⁺ ions into Fe-BDC results in long-range disorder with local crystallinity, which is beneficial to expose more active sites,¹⁴ and larger ECSA can be achieved. Second, proper incorporation of Ni²⁺ ions would strengthen the activity of the single site, as demonstrated by the highest value of the TOF, and it has been proposed that partial-charge exchange between Fe sites and Ni sites may happen in a bimetallic system,³⁵ thus enhancing the site catalytic activity. Third, fastest charge transfer as illustrated by the R_{ct} value would accelerate the reaction kinetics, which is verified by the lower Tafel slope.

The OER mechanism based on Fe1Ni2-BDC was also studied using the rotating ring-disk electrode (RRDE) technique. The Pt ring potential was set at 1.50 V vs RHE, ensuring that any generated peroxide intermediates (HO_2^-) on the catalyst surface could be oxidized during the OER process. As shown in Figure S5a, the ring current is about 7.5 μA , much lower than the disk current, demonstrating negligible generation of HO_2^- on the Fe1Ni2-BDC electrode, and the main reaction during the water oxidation is a standard four-electron process: $4\text{OH}^- \rightarrow \text{O}_2 + 2\text{H}_2\text{O} + 4\text{e}^-$. Faradaic efficiency was measured to further confirm that there are no other side reactions. To test the Faradaic efficiency, a ring potential of 0.40 V vs RHE was used to reduce the produced O_2 on the disk. In this way, it could realize the continual process from OER to ORR (oxygen reduction reaction). During this test, the generated O_2 from OER on the disk electrode will diffuse to the ring electrode where the ORR happens and O_2 is rapidly reduced. A ring current of $\sim 44.0 \mu\text{A}$ and a disk current of $\sim 0.24 \text{ mA}$ were collected, as shown in Figure S5b, and the Faradaic efficiency was calculated to be 99.5% (see detailed calculations in the Supporting Information), indicating the highly selective oxidation of water into O_2 .

The Fe1Ni2-BDC sample after a 2 h durability test was collected and characterized by ex situ TEM. The ex situ TEM image of Fe1Ni2-BDC after the OER test (Figure S10a) shows no obvious change when compared with the pristine sample, and the HRTEM image (Figure S10b) and SAED pattern (Figure S10c) still show ambiguous lattice fringes due to the low crystallinity. HAADF-STEM and EDX elemental images (Figure S10d–h) further confirm the uniform distribution of Fe and Ni after OER. These results suggest that the low-crystalline structure of Fe1Ni2-BDC is stable during the electrochemical testing, which could contribute to the excellent long-term stability.

The chemical states after a 2 h durability test were also characterized by ex situ XPS. As shown in Figure S11a, ignoring the strong F 1s signal from Nafion, the sample shows no distinct change of the XPS spectra after a 2 h durability measurement. In Figure S11b, the signal at 856.1 eV assigned to the Ni–O bonds is almost kept, except for the widening of the peak width, which is possibly due to the absorption of oxygen species or slight surface oxidation.³⁶ The phenomenon above can also be observed in C 1s (Figure S11d) and O 1s (Figure S11e) spectra, where the Fe(Ni)–O binding energy increases a little and the intensity of O–C=O decreases due to the mild change on the surface after the OER process. It should be indicated that due to the strong energy loss peak of F 1s close to the Fe 2p_{3/2} envelope (Figure S11c), the Fe 2p_{3/2} signal is overlapped and presented without further analysis.³⁷

In summary, Fe/Ni-based bimetallic low-crystalline MOFs with a tunable elemental ratio were designed via exotic ion induction into the Fe-MIL-88B for the first time. The formation of local crystallinity and long-range disorder of Fe_xNi_y-BDC is verified by both experimental and theoretical analysis. Due to the low-crystalline structure and tunable metal ratio, abundant active sites with improved activity and fast charge transfer for enhanced reaction kinetics are achieved. Specifically, a low overpotential of 260 mV at 10 mA cm⁻² and a Tafel slope of 35 mV dec⁻¹ are obtained, considerably surpassing that of noble metal-based oxide (IrO_2). Our study not only highlights the research of low-crystalline MOFs but also inspires new understanding of the development of highly efficient catalysts for energy conversion technologies.

■ ASSOCIATED CONTENT

Supporting Information

The Supporting Information is available free of charge on the ACS Publications website at DOI: 10.1021/acsenergylett.8b02345.

Experimental details (material synthesis and characterizations, DFT calculation details, electrochemical measurements) and supplemental figures and tables (PDF)

■ AUTHOR INFORMATION

Corresponding Authors

*E-mail: liangzhou@whut.edu.cn.

*E-mail: mlq518@whut.edu.cn.

ORCID

Kangning Zhao: 0000-0003-2916-4386

Liang Zhou: 0000-0001-6756-3578

Liqiang Mai: 0000-0003-4259-7725

Author Contributions

#J.L and W.H. contributed equally to this work.

Notes

The authors declare no competing financial interest.

■ ACKNOWLEDGMENTS

This work was supported by the National Key Research and Development Program of China (2016YFA0202603), the National Natural Science Foundation of China (51521001, 21673171, 51502226) and the National Natural Science Fund for Distinguished Young Scholars (51425204).

■ REFERENCES

- (1) Zhang, B.; Zheng, X.; Voznyy, O.; Comin, R.; Bajdich, M.; García-Melchor, M.; Han, L.; Xu, J.; Liu, M.; Zheng, L.; et al. Homogeneously Dispersed Multimetal Oxygen-Evolving Catalysts. *Science* **2016**, *352*, 333–337.
- (2) Fu, Q.; Wu, T.; Fu, G.; Gao, T.; Han, J.; Yao, T.; Zhang, Y.; Zhong, W.; Wang, X.; Song, B. Skutterudite-Type Ternary $\text{Co}_{1-x}\text{Ni}_x\text{P}_3$ Nanoneedle Array Electrocatalysts for Enhanced Hydrogen and Oxygen Evolution. *ACS Energy Lett.* **2018**, *3*, 1744–1752.
- (3) Huang, J.; Han, J.; Wang, R.; Zhang, Y.; Wang, X.; Zhang, X.; Zhang, Z.; Zhang, Y.; Song, B.; Jin, S. Improving Electrocatalysts for Oxygen Evolution Using $\text{Ni}_x\text{Fe}_{3-x}\text{O}_4/\text{Ni}$ Hybrid Nanostructures Formed by Solvothermal Synthesis. *ACS Energy Lett.* **2018**, *3*, 1698–1707.
- (4) Lee, Y.; Suntivich, J.; May, K. J.; Perry, E. E.; Shao-Horn, Y. Synthesis and Activities of Rutile IrO_2 and RuO_2 Nanoparticles for Oxygen Evolution in Acid and Alkaline Solutions. *J. Phys. Chem. Lett.* **2012**, *3*, 399–404.

- (5) Huang, Y.; Yang, R.; Anandhababu, G.; Xie, J.; Lv, J.; Zhao, X.; Wang, X.; Wu, M.; Li, Q.; Wang, Y. Cobalt/Iron(Oxides) Heterostructures for Efficient Oxygen Evolution and Benzyl Alcohol Oxidation Reactions. *ACS Energy Lett.* **2018**, *3*, 1854–1860.
- (6) Nai, J.; Yin, H.; You, T.; Zheng, L.; Zhang, J.; Wang, P.; Jin, Z.; Tian, Y.; Liu, J.; Tang, Z.; et al. Efficient Electrocatalytic Water Oxidation by Using Amorphous Ni-Co Double Hydroxides Nanocages. *Adv. Energy Mater.* **2015**, *5*, 1401880.
- (7) Liang, H.; Meng, F.; Cabán-Acevedo, M.; Li, L.; Forticaux, A.; Xiu, L.; Wang, Z.; Jin, S. Hydrothermal Continuous Flow Synthesis and Exfoliation of NiCo Layered Double Hydroxide Nanosheets for Enhanced Oxygen Evolution Catalysis. *Nano Lett.* **2015**, *15*, 1421–1427.
- (8) Chen, P.; Zhou, T.; Xing, L.; Xu, K.; Tong, Y.; Xie, H.; Zhang, L.; Yan, W.; Chu, W.; Wu, C.; et al. Atomically Dispersed Iron-Nitrogen Species as Electrocatalysts for Bifunctional Oxygen Evolution and Reduction Reactions. *Angew. Chem., Int. Ed.* **2017**, *56*, 610–614.
- (9) Ledendecker, M.; et al. The Synthesis of Nanostructured Ni₃P₄ Films and Their Use as a Non-Noble Bifunctional Electrocatalyst for Full Water Splitting. *Angew. Chem., Int. Ed.* **2015**, *54*, 12361–12365.
- (10) Fu, H. Q.; Zhang, L.; Wang, C. W.; Zheng, L. R.; Liu, P. F.; Yang, H. G. 1D/1D Hierarchical Nickel Sulfide/Phosphide Nanostructures for Electrocatalytic Water Oxidation. *ACS Energy Lett.* **2018**, *3*, 2021–2029.
- (11) Liu, Y.; Li, Q.; Si, R.; Li, G. D.; Li, W.; Liu, D. P.; Wang, D.; Sun, L.; Zhang, Y.; Zou, X. Coupling Sub-Nanometric Copper Clusters with Quasi-Amorphous Cobalt Sulfide Yields Efficient and Robust Electrocatalysts for Water Splitting Reaction. *Adv. Mater.* **2017**, *29*, 1606200.
- (12) Wang, Q.; Shang, L.; Shi, R.; Zhang, X.; Zhao, Y.; Waterhouse, G. I. N.; Wu, L. Z.; Tung, C. H.; Zhang, T. NiFe Layered Double Hydroxide Nanoparticles on Co,N-Codoped Carbon Nanoframes as Efficient Bifunctional Catalysts for Rechargeable Zinc-Air Batteries. *Adv. Energy Mater.* **2017**, *7*, 1700467.
- (13) Yu, L.; Yang, J. F.; Guan, B. Y.; Lu, Y.; Lou, X. W. Hierarchical Hollow Nanoprisms Based on Ultrathin Ni-Fe Layered Double Hydroxide Nanosheets with Enhanced Electrocatalytic Activity towards Oxygen Evolution. *Angew. Chem.* **2018**, *130*, 178–182.
- (14) Bennett, T. D.; Cheetham, A. K. Amorphous Metal-Organic Frameworks. *Acc. Chem. Res.* **2014**, *47*, 1555–1562.
- (15) Cai, G.; Zhang, W.; Jiao, L.; Yu, S. H.; Jiang, H. L. Template-Directed Growth of Well-Aligned MOF Arrays and Derived Self-Supporting Electrodes for Water Splitting. *Chem.* **2017**, *2*, 791–802.
- (16) Li, F.-L.; Shao, Q.; Huang, X.; Lang, J. P. Nanoscale Trimetallic Metal-Organic Frameworks Enable Efficient Oxygen Evolution Electrocatalysis. *Angew. Chem.* **2018**, *130*, 1906–1910.
- (17) Zhao, S.; Wang, Y.; Dong, J.; He, C.-T.; Yin, H.; An, P.; Zhao, K.; Zhang, X.; Gao, C.; Zhang, L.; et al. Ultrathin Metal-Organic Framework Nanosheets for Electrocatalytic Oxygen Evolution. *Nat. Energy* **2016**, *1*, 16184.
- (18) Wang, X. L.; Dong, L. Z.; Qiao, M.; Tang, Y. J.; Liu, J.; Li, Y.; Li, S. L.; Su, J. X.; Lan, Y. Q. Exploring the Performance Improvement of the Oxygen Evolution Reaction in a Stable Bimetal-Organic Framework System. *Angew. Chem., Int. Ed.* **2018**, *57*, 9660–9664.
- (19) Shen, J. Q.; Liao, P. Q.; Zhou, D. D.; He, C. T.; Wu, J. X.; Zhang, W. X.; Zhang, J. P.; Chen, X. M. Modular and Stepwise Synthesis of a Hybrid Metal-Organic Framework for Efficient Electrocatalytic Oxygen Evolution. *J. Am. Chem. Soc.* **2017**, *139*, 1778–1781.
- (20) Duan, J.; Chen, S.; Zhao, C. Ultrathin Metal-Organic Framework Array for Efficient Electrocatalytic Water Splitting. *Nat. Commun.* **2017**, *8*, 15341.
- (21) Scherb, C.; Schodel, A.; Bein, T. Directing the Structure of Metal-Organic Frameworks by Oriented Surface Growth on an Organic Monolayer. *Angew. Chem., Int. Ed.* **2008**, *47*, 5777–5779.
- (22) Serre, C.; Mellot-Draznieks, C.; Surble, S.; Audebrand, N.; Filinchuk, Y.; Ferey, G. Role of Solvent-Host Interactions That Lead to Very Large Welling of Hybrid Frameworks. *Science* **2007**, *315*, 1828–1831.
- (23) T  llez S, C. A.; Hollauer, E.; Mondragon, M. A.; Casta  o, V. M. Fourier Transform Infrared and Raman Spectra, Vibrational Assignment and Ab Initio Calculations of Terephthalic Acid and Related Compounds. *Spectrochim. Acta, Part A* **2001**, *57*, 993–1007.
- (24) Sun, F.; Wang, G.; Ding, Y.; Wang, C.; Yuan, B.; Lin, Y. NiFe-Based Metal-Organic Framework Nanosheets Directly Supported on Nickel Foam Acting as Robust Electrodes for Electrochemical Oxygen Evolution Reaction. *Adv. Energy Mater.* **2018**, *8*, 1800584.
- (25) Liang, R.; Jing, F.; Shen, L.; Qin, N.; Wu, L. MIL-53(Fe) as a Highly Efficient Bifunctional Photocatalyst for the Simultaneous Reduction of Cr(VI) and Oxidation of Dyes. *J. Hazard. Mater.* **2015**, *287*, 364–372.
- (26) Bordiga, S.; Lamberti, C.; Ricchiardi, G.; Regli, L.; Bonino, F.; Damin, A.; Lillerud, K. P.; Bjorgen, M.; Zecchina, A. Electronic and Vibrational Properties of a MOF-5 Metal-Organic Framework: ZnO Quantum Dot Behaviour. *Chem. Commun.* **2004**, 2300–2301.
- (27) Bae, S. H.; Kim, J. E.; Randriamahazaka, H.; Moon, S. Y.; Park, J. Y.; Oh, I. K. Seamlessly Conductive 3D Nanoarchitecture of Core-Shell Ni-Co Nanowire Network for Highly Efficient Oxygen Evolution. *Adv. Energy Mater.* **2017**, *7*, 1601492.
- (28) Chandra, V.; Park, J.; Chun, Y.; Lee, J. W.; Hwang, I. C.; Kim, K. S. Water-Dispersible Magnetite-Reduced Graphene Oxide Composites for Arsenic Removal. *ACS Nano* **2010**, *4*, 3979–3986.
- (29) Friebe, D.; Louie, M. W.; Bajdich, M.; Sanwald, K. E.; Cai, Y.; Wise, A. M.; Cheng, M. J.; Sokaras, D.; Weng, T. C.; Alonso-Mori, R.; et al. Identification of Highly Active Fe Sites in (Ni,Fe)OOH for Electrocatalytic Water Splitting. *J. Am. Chem. Soc.* **2015**, *137*, 1305–1313.
- (30) Wang, Z.; Li, J.; Tian, X.; Wang, X.; Yu, Y.; Owusu, K. A.; He, L.; Mai, L. Porous Nickel-Iron Selenide Nanosheets as Highly Efficient Electrocatalysts for Oxygen Evolution Reaction. *ACS Appl. Mater. Interfaces* **2016**, *8*, 19386–19392.
- (31) Wang, M.; Lin, M.; Li, J.; Huang, L.; Zhuang, Z.; Lin, C.; Zhou, L.; Mai, L. Metal-Organic Framework Derived Carbon-Confined Ni₂P Nanocrystals Supported on Graphene for an Efficient Oxygen Evolution Reaction. *Chem. Commun.* **2017**, *53*, 8372–8375.
- (32) Yang, Y.; Fei, H.; Ruan, G.; Xiang, C.; Tour, J. M. Efficient Electrocatalytic Oxygen Evolution on Amorphous Nickel-Cobalt Binary Oxide Nanoporous Layers. *ACS Nano* **2014**, *8*, 9518–9523.
- (33) Liu, W.; Liu, H.; Dang, L.; Zhang, H.; Wu, X.; Yang, B.; Li, Z.; Zhang, X.; Lei, L.; Jin, S. Amorphous Cobalt-Iron Hydroxide Nanosheet Electrocatalyst for Efficient Electrochemical and Photo-Electrochemical Oxygen Evolution. *Adv. Funct. Mater.* **2017**, *27*, 1603904.
- (34) Sun, S.; Li, H.; Xu, Z. J. Impact of Surface Area in Evaluation of Catalyst Activity. *Joule* **2018**, *2*, 1024–1027.
- (35) Ma, W.; Ma, R.; Wang, C.; Liang, J.; Liu, X.; Zhou, K.; Sasaki, T. A Superlattice of Alternately Stacked Ni-Fe Hydroxide Nanosheets and Graphene for Efficient Splitting of Water. *ACS Nano* **2015**, *9*, 1977–1984.
- (36) Wang, H. Y.; Hsu, Y. Y.; Chen, R.; Chan, T. S.; Chen, H. M.; Liu, B. Ni³⁺-Induced Formation of Active NiOOH on the Spinel Ni-Co Oxide Surface for Efficient Oxygen Evolution Reaction. *Adv. Energy Mater.* **2015**, *5*, 1500091.
- (37) Grosvenor, A. P.; Kobe, B. A.; Biesinger, M. C.; McIntyre, N. S. Investigation of Multiplet Splitting of Fe 2p XPS Spectra and Bonding in Iron Compounds. *Surf. Interface Anal.* **2004**, *36*, 1564–1574.